The force balance of hydrogen bubbles growing and oscillating on a microelectrode

Hossain, S. S.; Bashkatov, A.; Yang, X.; Mutschke, G.; Eckert, K.;

Originally published:

September 2022

Physical Review E 106(2022), 035105

DOI: https://doi.org/10.1103/PhysRevE.106.035105

The force balance of hydrogen bubbles growing and oscillating on a microelectrode

Syed Sahil Hossain,[1] Aleksandr Bashkatov,[1,2] Xuegeng Yang,[1,2] Gerd Mutschke,[1,*] and Kerstin Eckert[1,2,3,†]

[1] *Institute of Fluid Dynamics, Helmholtz-Zentrum Dresden-Rossendorf, Bautzner Landstrasse 400, Dresden, 01328 Germany*

[2] *Hydrogen Lab, School of Engineering, Technische Universität Dresden, Dresden, 01062, Germany*

[3] *Institute of Process Engineering and Environmental Technology, Technische Universität Dresden, Dresden, 01062 Germany*

(Dated: September 7, 2022)

Hydrogen evolution in acidic aqueous electrolytes was recently found to be characterized by a carpet of microbubbles covering the microelectrode and feeding the growth of the main bubbles by coalescence. Besides this, oscillatory behavior of the main bubbles was observed prior to departure. Extending earlier studies, this work delivers the forces acting on the main bubble more accurately by taking into account further geometric and electrochemical details measured during experiments. Combining simulation work and measurements makes it possible to confirm the role of an attractive electrical (Coulomb) force caused by the adsorption of hydrogen ions at the bubble interface and to obtain a better understanding of the bubble dynamics observed.

I. INTRODUCTION

With the increasing urgency of a clean energy transition, the use of H_2 as an energy storage solution for renewable sources is a subject of intense investigation and investment [1–3]. One promising pathway is obtaining H_2 from the electrolysis of water [4–6]. Though this process has been known for a long time and alkaline water electrolysis is a mature technology [7], there is still a lack of understanding details of the electrolytic evolution of gas bubbles, such as precisely predicting the instant of departure from the electrode or bubble coalescence. As these details are of importance with respect to the efficiency of technical devices, there has been increased activity in gaining an improved understanding of electrolytic bubble dynamics.

In general, the dynamics of an electrolytic bubble is determined by the magnitude, direction and characteristics of all forces acting on it. For an extensive review of forces and bubble detachment models existing so far we refer to Thorncroft and Klausner [8]. When considering a bubble growing on a horizontal electrode, the vertical force components determine the departure dynamics. As the radius R_b of the bubble continuously grows during electrolysis, the buoyancy force $\sim R_b^3$ acting on the bubble in upward direction strongly increases. At a certain instant of time the upward forces will then overcome the downward forces, and the bubble attempts to detach. This typically happens without delay by continuous bubble rise. However, recently at large negative potentials it was observed at microelectrodes (see FIG. 1) that the bubbles undergo a period of vertical position oscillations prior to detachment. This new mode of departure dynamics was found to be caused by forces originating from Marangoni and electric effects that were only little considered before [9]. Therefore, Marangoni and electric forces have recently attracted great interest to gain a deeper insight into the dynamics of electrolytic gas bubbles [10–16].

Marangoni effects originate from a surface tension gradient along liquid or gaseous material interfaces [17]. When this gradient is caused by a gradient in temperature, it is also known as the thermocapillary effect. A brief overview of studies on thermocapillary effects on bubbles in general and in the context of electrolysis is provided in the following. Young et al. [18] demonstrated the importance of the thermocapillary effect on a bubble in a temperature field for the first time by showing that a vertical temperature gradient may be used to levitate a bubble against buoyancy. They also obtained good agreement with the analytical prediction of the required temperature gradient. By means of numerical computation, Larkin [19] calculated the details of the thermocapillary flow adjacent to a hemispherical bubble residing on a heated solid wall. Kao and Kenning [20] extended the computations of the thermocapillary flow around a bubble residing on a heated wall to include a wider range of process parameters that were expressed in dimensionless numbers, namely the Marangoni number (Ma), Rayleigh number (Ra) and Biot number (Bi). They also showed that the thermocapillary flow is highly sensitive to the presence of even small amounts of surface-active contaminants. Kassemi and Rashidnia [21] showed that the thermocapillary flow around a pendant bubble attached to a heated wall exhibits oscillatory and non-oscillatory behavior depending on Ma. They also showed that the oscillatory nature of the thermocapillary flow undergoes a transition from transverse to axial flow oscillations at an

* g.mutschke@hzdr.de

† k.eckert@hzdr.de

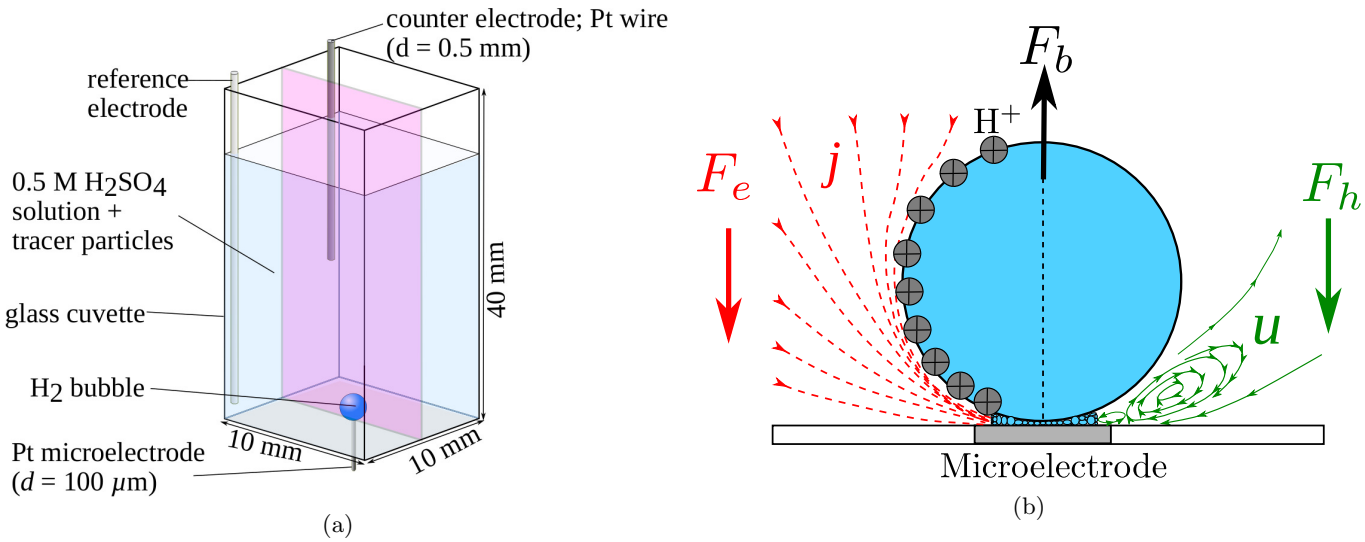

FIG. 1: (a) Sketch of the electrolysis cell (Updated from Ref [12]). The central plane is shown in pink. (b) Zoomed view in the central plane of an electrogenerated bubble growing on a carpet of microbubbles with associated interfacial phenomena and acting forces.

analytically predictable critical Ma. Later, Lubetkin [22] also discussed the possible combined effect of soluto- and thermocapillary forces and buoyancy on the oscillation of a bubble levitated in a vertical thermal gradient. Guelcher et al. [23] were the first to consider thermocapillary effects at electrogenerated gas bubbles. They attributed the horizontal bubble movement observed also earlier by Tobias and Sides [24] to a possible thermocapillary effect by calculating the thermocapillary flow around a bubble in the close vicinity of a heated wall, similarly to Ref [19, 20]. However, direct experimental evidence of the thermocapillary effect was still lacking, as neither the temperature distribution nor the fluid flow around the gas bubble were ever measured. By means of particle tracking velocimetry (PTV), Yang et al. [11] were the first to measure the fluid flow in the vicinity of H_2 bubbles grown on a Pt microelectrode. In order to clarify the relation to thermocapillarity, Massing et al. [12] carried out simultaneous measurements of temperature and electrolyte flow close to the bubble and compared the observations with numerical computation, which allowed them to confirm the thermocapillary effect. As sketched in Fig. 1(b), the large current density at the wetted outer edge of the microelectrode creates a lateral temperature gradient along the bubble interface, which drives a corresponding recirculating flow [11, 12]. This flow structure is responsible for the hydrodynamic force experienced by the bubble. Later, Hossain et al. [13] further extended the study by investigating bubbles growing at electrodes of varying sizes. Recently, Meulenbroek et al. [14] showed that assuming the existence of surface-active contaminants that might have been present during the measurements of Massing et al. allows to further improve the quantitative agreement between the flow profiles obtained in experiments and computations.

In addition to Marangoni effects, Lubetkin [25, 26] hypothesized that an electric force could affect the dynamics of an electrogenerated bubble. It has been known for a long time that bubble interfaces are electrically charged [27–29]. Multiple studies have quantified the electric nature of the bubble interface by calculating the ζ potential based on electrophoretic measurements [30–33]. Brandon et al. [34] quantified the electric charge of a H_2 bubble generated in a water electrolysis cell. Recently, Bashkatov et al. [9] observed a regime of oscillatory bubble growth above a carpet of microbubbles at microelectrodes which also relates to previous observations [24, 35]. They proposed and provided a working mechanism for the oscillation as competition between the electric and Marangoni force and the buoyancy force acting on the bubble [9]. Since the electrogenerated bubble grows in an electrolyte medium, the bubble interface is electrically charged depending on the solution pH [31, 34, 36–40]. For the strongly acidic electrolyte used it is therefore argued that the electric force is caused by the adsorption of hydrogen ions at the bubble interface (see FIG. 1(b)). As the bubble interface becomes positively charged, the bubble is attracted in the electric field towards the cathode. Applying a simplified modeling approach, an initial quantification of the interfacial charge density was obtained utilizing the force balance at equilibrium. The value obtained was found to be in good agreement with literature values [30, 41]. This made it possible to quantify the electric force acting on an electrogenerated bubble. Finally, the variation of the electric force with the bubble position was used to explain the observed position oscillations of the bubble.

For the potentiostatic growth mode studied in Ref [9], FIG. 2 shows the typical temporal behavior of the cell current (I) and bubble position during the life cycle of a single bubble, where the bubble evolves with oscillations at a late

stage. H^* is the vertical distance between the top of the bubble and the electrode surface normalized by the bubble diameter. Bashkatov et al. [9] showed that the oscillations in bubble position and cell current are related to each other and are exactly out of phase.

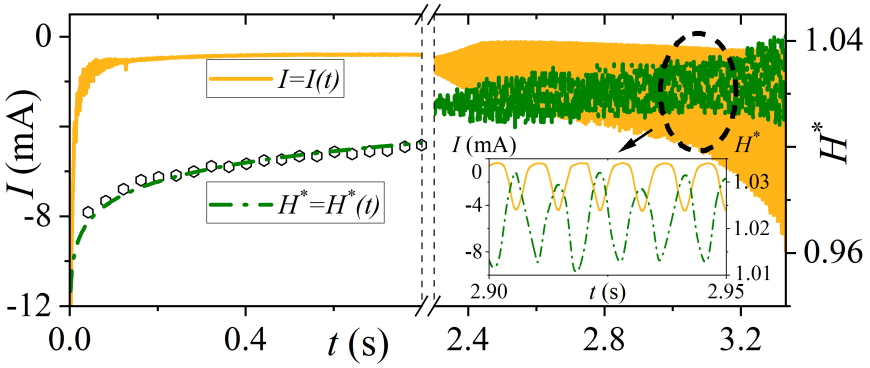

FIG. 2: Example of an oscillatory bubble evolution at a microelectrode (reprinted from Ref [9])

In the present study, we build on previous works, namely Ref [9, 12, 14], to provide an improved modeling and understanding of the forces acting on H_2 bubbles grown on microelectrodes and their dynamics. In detail, the modeling of the bubble dynamics now includes the pressure part of the hydrodynamic force [14] neglected earlier [9, 12]. Furthermore, motivated by high-speed camera images of the oscillatory bubble evolution, bubble deformation effects that may become important at large pontentials (see Fig. 3) will firstly be taken into account in the advanced modeling approach. The simulation methodology presented will also consider a time-varying insulating effect of the gas carpet on the electrode surface during the bubble dynamics. Both the stationary and oscillatory growth regimes are taken into account when estimating the surface charge density in force equilibrium and comparing it with earlier work [9]. For the oscillatory regime, the temporal variation of the different forces acting on the bubble is investigated in detail during one oscillation cycle. Beside the modeling work, flow velocities measured by particle tracking velocimetry during the bubble oscillation are presented, and a comparison is drawn between the experiment and computation.

The paper is organized as follows: Section II contains a quantitative description of the forces acting on the bubble. Section III describes the simulation approach and the experimental method applied, emphasizing the improvements compared to earlier work. The application of the force equilibrium condition for a stationary bubble is discussed in Section IV A, and the forces acting on an oscillating bubble are discussed in Section IV B. Finally, in the Conclusion we discuss the implications and possibilities of future work, and additional information on the methods is provided in the Appendices.

II. FORCES ACTING ON THE BUBBLE

In general, the dynamics of an electrogenerated bubble can be described by Newton's law

$$m_b \vec{a} = \vec{F} = \sum_i \vec{F_i} \tag{1}$$

where m_b, $\vec{a}$ and $\vec{F}$ denote the bubble mass, its acceleration and the total force, which may in general consist of several individual forces $\vec{F_i}$. Overhead arrows are used to denote vector quantities. For a detailed review of the forces on bubbles we refer to Thorncroft and Klausner [8]. In the following, we consider and quantify the forces only that are applicable to our electrolysis system sketched in FIG. 1 where a bubble grows on a microelectrode. As our system possesses axisymmetry, only the vertical force components are considered in the following to analyze the detachment dynamics.

The buoyancy and the hydrodynamic force are obtained from integrating the surface stress $\vec{\tau} = \mathbf{T} \cdot \hat{n}$ over the bubble-electrolyte interface $\mathcal{S}$, where $\mathbf{T} = -p\mathbf{I} + \mu(\nabla \vec{u} + \nabla \vec{u}^T)$ is the stress tensor and p is the total pressure. $\hat{n}$ is the surface normal unit vector and $\vec{u}$ is the flow velocity vector. The total pressure, p, can be split into static (p_s) and dynamic (p_h) parts, i.e., $p = p_s + p_h$. The integral of p_s over the bubble interface gives the buoyancy force

$$F_b = V_b \left(\rho_l - \rho_g\right) g, \tag{2}$$

where ρ_l, ρ_g and V_b denote the density of the liquid and the gas phase and the bubble volume, respectively. The remaining hydrodynamic boundary stress [42],

$$\overrightarrow{\tau_h} = -p_h\hat{n} + \mu\frac{\partial\overrightarrow{u}}{\partial n} + \mu\nabla u_n \tag{3}$$

can be split into a pressure part and a viscous part. Thus we obtain the pressure force,

$$\overrightarrow{F_p} = -\int_{\mathcal{S}} p_h\hat{n}\,\mathrm{d}A \tag{4}$$

originating from the variation in the hydrodynamic pressure along the interface, and the viscous force,

$$\overrightarrow{F_v} = \mu\int_{\mathcal{S}}\left(\frac{\partial\overrightarrow{u}}{\partial n} + \nabla u_n\right)\mathrm{d}A \tag{5}$$

The total hydrodynamic force on the bubble is then given given by

$$\overrightarrow{F_h} = \overrightarrow{F_p} + \overrightarrow{F_v} = \int_{\mathcal{S}}\overrightarrow{\tau_h}\,\mathrm{d}A \tag{6}$$

As we are dealing with an axisymmetric system, the integrals only provide non-zero vertical components,

$$F_h = F_p + F_v \tag{7}$$

At the bubble interface between the gas and liquid phases, the stress balance needs to be satisfied [17],

$$(\mathbf{T}^l - \mathbf{T}^g)\cdot\hat{n} + \nabla_S\gamma - \gamma\hat{n}(\nabla\cdot\hat{n}) = 0 \tag{8}$$

where γ is the interfacial tension and $\nabla_S \equiv \nabla - \hat{n}\,(\hat{n}\cdot\nabla)$ is the surface gradient operator. The superscripts l and g represent the liquid and the gas phase, respectively. Taking the inner product with the normal and tangential unit vectors, Eq. 8 can further be divided into the normal stress balance,

$$p^g - p^l + 2\mu^l\frac{\partial u_n^l}{\partial n} = \gamma\,(\nabla\cdot\hat{n}) \tag{9}$$

and the tangential stress balance,

$$\mu^l\frac{\partial u_t^l}{\partial n} = -\nabla_S\gamma\cdot\hat{t} \tag{10}$$

where in the latter the gas viscosity was assumed to be comparatively small. Since the surface tension γ in general depends on temperature, thermocapillary stress, $\tau_M = \nabla_S\gamma\cdot\hat{t}$ arises from temperature differences along the bubble interface. For the cases considered in the following, the temperature influence dominates, and the additional influence of pH variations on the surface tension that may arise from the electrochemical reaction can be safely neglected [43]. Therefore, in our model a linear dependence of γ on temperature T is assumed, i.e. $\gamma\,(T) = \gamma_0 + \beta T$, where β is the temperature coefficient of the interfacial tension. The resulting force on the bubble can be calculated as $F_M = -\int_{\mathcal{S}}\tau_M\mathrm{d}A$ and was denoted as Marangoni force in Ref [9, 12, 13] Taking the inner product of Eq. 3 with $\hat{t}$, it can also be seen that the left-hand side of Eq. 10 is the tangential component of $\overrightarrow{\tau_h}$. Thus F_M essentially captures the contribution from the tangential stress at the interface. The contribution from the normal stress can be obtained by integrating the normal component of the hydrodynamic boundary stress, $F_n = \int_{\mathcal{S}}\tau_{h,n}\mathrm{d}A$ and $\tau_{h,n} = \overrightarrow{\tau_h}\cdot\hat{n} = -p_h + 2\mu^l\frac{\partial u_n}{\partial n}$. Thus, $F_h = F_M + F_n = F_v + F_p$.

If the electrogenerated bubble grows in an electrolyte medium, the bubble interface may become electrically charged [31, 34, 36–40]. As the pH value of the electrolyte used in our experiments is below the isoelectric point [30, 41], the surface charge density is positive, primarily due to H^+ ion adsorption at the interface. As can be expected from the electric current density vectors encasing the bubble (see FIG. 1 (b)), the resulting electric field in the bubble vicinity causes an electric force F_e on the bubble, as recently discussed in [9]. It is given as

$$F_e = \int_{\mathcal{S}}\sigma E_z\,\mathrm{d}A \tag{11}$$

E_z is the vertical (z) component of the external electric field, $\mathcal{S}$ is the interface between bubble and electrolyte, and σ is the surface charge density of the bubble interface. As will be shown below, both the electric force and the

hydrodynamic force depend on the vertical bubble position abive the microelectrode (see also [44]).
For the time range and operational parameters investigated in the following, the H_2 bubble grows on a thin layer of continuously evolving gas and is not in contact with the electrode [9]. Henceforth, the contact force acting on the three-phase contact line by virtue of the surface tension and also the contact pressure force due to an excess pressure acting on the attached area of the bubble do not apply [8, 25, 45]. Instead, a possible force contribution may result from the interaction between the gas layer and the gas bubble, which could be understood as a body force acting on the bubble. Since the gas carpet is a collection of very small bubbles with thin electrolyte films between them, the carpet-bubble interaction can be described by the concept of disjoining pressure [46, 47]. Though a detailed quantification is left for future studies, we expect the carpet-bubble interaction to be small close to detachment and therefore neglect it in the following.
Finally, in general a further contribution to the hydrodynamic force arises due to the growth of the bubble with time [48]. However, as we are dealing with the late stage of bubble evolution when the bubble growth rate is very small [12], for the short periods of time considered in the simulations below, such effects can be safely neglected. For completeness we also note that if the water electrolysis is carried out in an accelerating reference frame, e.g., during parabolic flights, additionally corresponding fictitious forces need to included in the equation of motion [49]. In summary, equation (1) can be written as

$$m_b\, a = F = F_b + F_h + F_e \tag{12}$$

As will be described in the following section, the computational approach for calculating the bubble dynamics consists of considering a bubble at fixed position and performing transient simulations from a resting electrolyte at ambient temperature for a certain period of time to allow for the flow and the temperature profiles at the bubble to reach a quasistationary regime. As this approach neglects the effects of accelerated bubble motion, forces accounting for acceleration need additionally to be considered, which are the added mass force and the history force [50]. Thus, the equation of motion can be further specified to

$$(m_b + m_a)\, a \approx F_b + F_h + F_e + F_{hs} \tag{13}$$

The mass of the bubble $m_b = V_b \rho_g$ results from the bubble volume V_b and the density of the gas ρ_g. In the calculation, the density of air at atmospheric pressure is used. The added mass m_a accounts for the effort of accelerating the nearby fluid and essentially slows down a transient change of bubble velocity. For a sphere moving in a large fluid media, the added mass is half of the displaced fluid mass $m_a = 0.5 V_b \rho_f$ [51], where ρ_f is the density of the fluid. Since $\rho_g \ll \rho_f$, $m_b \ll m_a$. The history force F_{hs}, also known as the Basset force, originates from the unsteadiness of the fluid flow as well and additionally accounts for the time history of the flow conditions nearby [52]. A general formulation of the history force is given by [52],

$$F_{hs}(t) = 6\pi\mu R_b \int_{-\infty}^{t} K(t-s) \frac{\mathrm{d}(V-U)}{\mathrm{d}s} \mathrm{d}s\,. \tag{14}$$

Here, V is the flow velocity, U is the bubble velocity, and K is the kernel function which depends on the exact flow configuration. Various kernel functions and computation methods have been proposed; for more detail see [52–54]. Combining the discussion above, the equation of motion of the bubble can be given by

$$m_a\, a \approx F_b + F_h + F_e + F_{hs} \tag{15}$$

When the bubble is at a force equilibrium, the acceleration of the bubble is zero, i.e., $a = 0$ and Eq. 15 then becomes

$$F_b + F_h + F_e + F_{hs} \approx 0 \tag{16}$$

III. METHODS

A. Simulation

FIG. 3a shows a representative shadowgraph image of a H_2 bubble on a Pt microelectrode, and FIG. 3b specifies the corresponding computational domain (axi-symmetric) used in this study. It can be seen in FIG. 3a that the bubble is situated on a layer of microbubbles that are continuously generated by the hydrogen evolution reaction at the cathode. Depending on the experimental details, the layer thickness (denoted by δ) and its radial extension (denoted by R_g) may vary. In the simulations, the layer, as shown in green in FIG. 3b, is assumed to homogeneously

consist of gas only. The gas bubble growing on the gaseous carpet by coalescence with the microbubbles is shown in blue in FIG. 3b and has the radius R_b. A deformation from the circular shape can be observed in the lower bubble part in FIG. 3a. This deformation will be denoted by ε in the following. As ε may become larger than δ (see also [9]), this detail is important and will be firstly considered in the simulations. The bubble deformation is implemented in the model in a simplified manner by drawing a tangent to the spherical bubble from the outer corner of the gas layer. The gas coverage of the cathode can be defined as

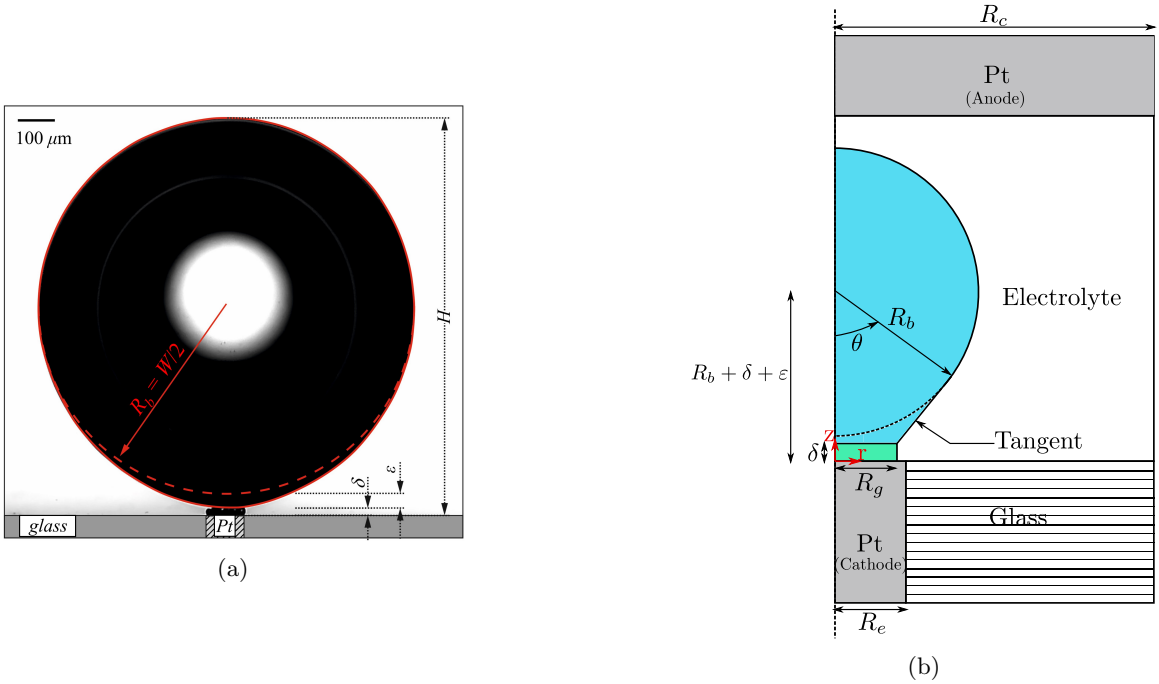

FIG. 3: (a) Representative image of the bubble captured during its position oscillations, at instance of the last top position before detachment, with $R_b = 498\ \mu$m, $\delta = 16\ \mu$m and $\varepsilon = 37\ \mu$m. The experiment was performed in 0.5 M H_2SO_4 at -7 V. The instance of time is marked in FIG 5b with a blue vertical line at t=2.486 s. (b) Setup for the axi-symmetric simulations (not to scale). The vertical dotted line denotes the axis of rotation.

$$\Theta = \left(\frac{R_g}{R_e}\right)^2 \times 100 \tag{17}$$

where R_e denotes the electrode radius. Varying the radius of the gas layer can be expected to strongly affect the total resistance of the cell to the electric current. We note here that considering the gas carpet to be a uniform gas layer in the model is an approximation, whereas in reality it consists of a large number of microbubbles feeding the bigger 'mother' bubble. Therefore, Θ as defined and used in the model is meant to capture the net insulating effect of the gas layer on the microelectrode, even though the detailed description might differ. Since the net electrode coverage is difficult to extract with reasonable accuracy from the shadowgraph images, Θ is implemented as a model parameter. Thus, R_b, δ and ε are taken from measurements, and R_g is adjusted jointly with the cell voltage in the simulations to match the cell current, as described below. Finally, R_c denotes the inner radius of the cell, and θ is the angular position along the bubble interface.

Next, the simulation methodology is briefly sketched. As it closely resembles earlier work, for further details we refer to [9, 13]. The computational domain is shown in FIG. 3b. The bubble interface is assumed to be non-deformable, hence the Navier-Stokes equation (Eq. 18c) and the continuity equation (Eq. 18b) are only solved in the electrolyte. The bubble is kept at a fixed position in both the stationary and the oscillatory growth modes. The electric current in the cell provides a source of heat in the electrolyte, which is convected and conducted throughout the cell. Eq. (18d) is the heat equation solved in the electrolyte. The last term ($|\vec{j}|^2/\sigma_e$) captures the Joule heating due to electric current. A Laplace equation of the electric potential (ϕ) is solved in the electrolyte.The electric potential distribution is required to calculate the electric current density distribution $\vec{j} = -\sigma_e \nabla\phi$ in the cell, which is used to calculate the non-uniform rate of heat generation in the electrolyte. σ_e denotes the electrical conductivity of the electrolyte. Thus,

the governing equations to be solved in the electrolyte are

$$\nabla^2\phi = 0 \tag{18a}$$

$$\nabla \cdot \overrightarrow{u} = 0 \tag{18b}$$

$$\rho\left(\frac{\partial \overrightarrow{u}}{\partial t} + (\overrightarrow{u}\cdot\nabla)\overrightarrow{u}\right) = -\nabla p + \mu\nabla^2\overrightarrow{u} \tag{18c}$$

$$\rho C_p\left(\frac{\partial T}{\partial t} + (\overrightarrow{u}\cdot\nabla)T\right) = k\nabla^2 T + \frac{|\overrightarrow{j}|^2}{\sigma_e} \tag{18d}$$

where $\overrightarrow{u}$ is the flow velocity vector, p is the pressure, ρ is the electrolyte density, μ is the viscosity of the fluid, C_p is the specific heat of the fluid, T is the temperature and k is the thermal conductivity. In all other domains, namely the electrodes, the glass cuvette and the bubble, only the transient heat diffusion equation is solved:

$$\rho\, C_p\, \frac{\partial T}{\partial t} = k\nabla^2 T \tag{19}$$

Next we discuss the boundary conditions. Temperature boundary conditions are needed at the outer boundaries of the entire computational domain and at the symmetry axis. At the right edge of the computational domain, an adiabatic boundary condition $\partial T/\partial n = 0$ is applied, whereas the top and bottom edges are maintained at ambient temperature $T = T_{amb}$. At the left side, for the symmetry axis $\partial T/\partial n = 0$ applies.

Since the Eq.s 18 are solved only in the electrolyte domain, the boundary conditions are needed only at the respective boundaries. For Eq. 18a the boundary conditions are as follows: at the anode suface it holds $\phi = \Delta\phi_{sim}$, and at the cathode surface exposed to the electrolyte it holds $\phi = 0$. All other boundaries are insulating i.e. $\partial\phi/\partial n = 0$. We note here that $\Delta\phi_{sim}$ is varied with Θ such that the cell current measured (I_{exp}) in the experiment matches the simulation (I_{sim}). Further details on the choices made will be described below.

For the fluid flow, at the boundaries that represent the interface between gas and electrolyte, the tangential stress balance of Eq. 10 is applied along with a free slip boundary condition. The surface tension is taken to be a linear function of temperature. Since the temperature rise we deal with is not too large (see below, [12]), this model gives a realistic distribution of surface tension along the interface. At the remaining boundaries, a no-slip condition applies.

Eq.s 18 along with the boundary conditions are solved by using the FEM package COMSOL 5.5. The electrolyte has the initial conditions of $\overrightarrow{u} = 0$, $p = 0$ and $\phi = 0$, and the whole domain is initially at ambient temperature $T_{amb} = 25^oC$. The computations are carried then out for a period of 1 s until which a quasi-stationary regime has built up in the vicinity of the bubble [12]. To better motivate the computational approach, in the following relevant time-scales and non-dimensional parameters are analyzed. The time scales of various transport mechanisms can be obtained as follows: advection time scale, $t_a = R_b/U$, momentum diffusion time scale, $t_m = R_b^2/\nu$ and thermal diffusion time scale, $t_{th} = R_b^2\rho c/k$. When using a representative velocity value of $U = 50$ mm/s, a bubble radius of $R_b = 0.5$ mm and the material properties given in Appendix C, Table I summarizes the relevant time scales. As can

t_a (s)	t_m (s)	t_{th} (s)	t_o (s)
0.01	0.3	2.1	0.01

TABLE I: Relevant timescales

be seen, momentum advection is much faster than momentum diffusion, but after 1 s a quasi-stationary regime can be assumed to be obtained. As thermal diffusion will come into effect only later, the simulations over 1 s are expected to capture the dominant transport physics. However, in the case of bubble oscillations, a lateral oscillation frequency of the bubble of about 100 Hz can be assumed [9]. Thus, the oscillation time scale (t_o) is quite small, and the results obtained should be interpreted with care, as obviously the effect of oscillatory transients on the transport physics is not fully resolved.

Important nondimensional parameters of the problem are the Reynolds number characterizing the flow driven around the gas bubble, the Péclet number characterizing the ratio of heat advection and diffusion, and the Marangoni number characterizing the importance of thermocapillary effect. As known from the current and also earlier simulations, large current density values of about $|\overrightarrow{j}| \sim 10^7$ A/m^2 are found near the outer edge of the cathode where the

temperature hotspot occurs [13]. When using $\Delta T = 20$ K as a representative value for the local temperature rise [12], we obtain $Re = \frac{\rho U R_b}{\mu} \approx 25$, $Pe = \frac{U R_b}{\alpha} \approx 180$ and $Ma_{th} = -\frac{\beta \Delta T R_b}{\mu \alpha} \approx 10^4$, where $\nu = \frac{\mu}{\rho}$ is the kinematic viscosity and $\alpha = \frac{k}{\rho C_p}$ is the thermal diffusivity of the electrolyte. We see from the Reynolds number that the electrolyte flow can be expected to be laminar, but since $Re > 1$ the inertia term can not be neglected in Eq. 18c. The large Péclet number points to the dominant nature of convective heat transfer in the electrolyte, and the very large Marangoni number clearly emphasizes the thermocapillary effect as the primary driving factor of the electrolyte flow. We finally mention that, for the short integration times considered, the effect of solutal buoyancy may safely be neglected [12].

In order to validate the computational approach, a characteristic temporal behavior of the forces calculated is shown in FIG. 4. As can be seen, the values quickly reach a plateau and thus represent a quasi-stationary estimate of forces. We also draw attention to the magnitudes of the forces. It can be seen in FIG. 4 that $F_h = F_n + F_M = F_p + F_v$, as already discussed in Section II. We can also see that F_p is an important contributing factor to F_h [14], and thus to the force balance of the bubble.

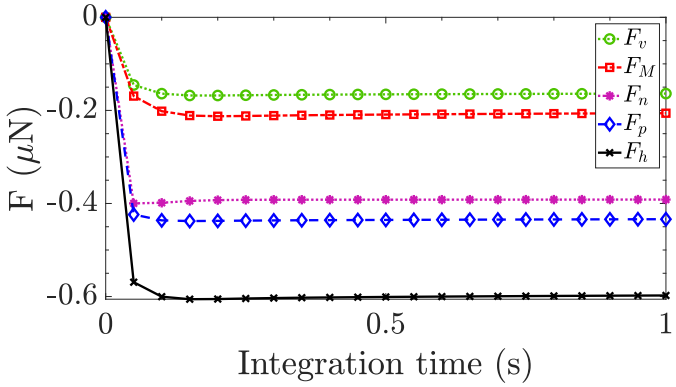

FIG. 4: Time characteristics of the calculated forces for case (a) of Table II

B. Experiment

The experiments were performed in an electrolysis cell that is sketched and dimensioned in FIG. 1a. The bubble evolution and the electrolyte velocity were measured using shadowgraphy and micro-particle tracking velocimetry (μPTV). The electrochemical setup is similar to [12, 55]. A Pt wire acts as a pseudo-reference electrode (≈ 0.48 V vs. reversible hydrogen electrode RHE for 0.5 M H_2SO_4). The electric potential of the working electrode with respect to the reference electrode is henceforth referred to as ϕ_c. The cell voltage, given by the difference of anode and cathode potential, is $\Delta\phi_{exp} = \phi_a - \phi_c$, where ϕ_a is the potential of the anode with respect to the reference electrode. We also use the subscripts *'exp'* and *'sim'* to draw attention to the difference in the same quantity between measurement and simulation.

A Zahner electrochemical workstation is used to operate the cell in potentiostatic mode, i.e., with constant electric potential of the working electrode with respect to the reference electrode. During the experiments, for a time period of 30 s, the electric current was recorded with a sampling rate of 1 kHz or 2 kHz when using either shadowgraphy or PTV, respectively.

The PTV setup consists of a green laser (Photonics, Nd:YLF 527 nm, 20 mJ) and a high-speed camera (Phantom, VEO 410L) connected to a stereo microscope (ZEISS, SteREO Discovery.V8), closely resembling Ref [11, 12]. The laser is connected to the microscope via a glass fiber. The frame rate of the camera is 2 kHz and the spatial resolution of the microscope system is 307 pix/mm. A concentration of 0.009 % w/v monodisperse fluorescent polystyrene particles (microParticles GmbH, PS-FluoRed, 530 nm/607 nm) of 5 μm diameter were seeded into the electrolyte. The particles have a density of $\rho_{PS} = 1.05\ g/cm^3$, making them neutrally buoyant. The green laser light passes through the electrolysis cell placed in front of the microscope, through the glass fiber connected to the side of the microscope, i.e., providing a volumetric illumination. The fluorescent particles adsorb the green light and re-emit red light , which goes back to the microscope and to the camera sensor via a band-pass filter. The series of images of the particles provided over a time interval are processed by the commercial PTV software DaViS 10, yielding a two-component velocity of each particle over time. Because of the fast bubble oscillation frequency of about 100 Hz, the resultant tracks of the particles were calculated over 5 to 10 images and then averaged over several bubbles.

Shadowgraphy was used to capture high-resolution images of the bubble evolution with time. The shadowgraphy system consists of the high-speed camera (IDT Os7 - S3) connected to a microscope (Thalheim SpezialOptik Pulsnitz, Germany), providing a spatial resolution of 1000 pix/mm. An LED light illuminates the electrolysis cell, which is placed between the camera and the light source. The image recording was carried out at a frame rate of 1 kHz. A picture is shown by way of example in FIG. 3a. These images were analyzed to obtain the geometric features of the bubble (R_b, δ, ε). To ensure that conditions were similar between the shadowgraphy and μPTV measurements, the same amount of fluorescent particles was added to the solution for the shadowgraphy experiments.

IV. RESULTS & DISCUSSION

In this section, we discuss specific time instants of two characteristic bubble evolution regimes, applying the simulation and measurement methods described in the previous section. Depending on the electrolyte concentration (c) and the electrode potential (ϕ_c) applied, different regimes of bubble evolution are observed in the experiments. Generally, in lower c and at lower ϕ_c, the bubble is observed to grow steadily until it simply detaches, whereas at higher values of c and ϕ_c it is seen to undergo position oscillations prior to detachment [44]. These two regimes are reflected in the temporal behavior of the cell current measured over the lifetime of the bubble. Steady growth and departure can be seen in FIG. 5a, whereas in FIG. 5b, the regime during growth changes from stationary to oscillatory bubble dynamics, as seen from the fact that the current oscillations grow with time in the second half of the bubble cycle.

A. Non-oscillating bubble

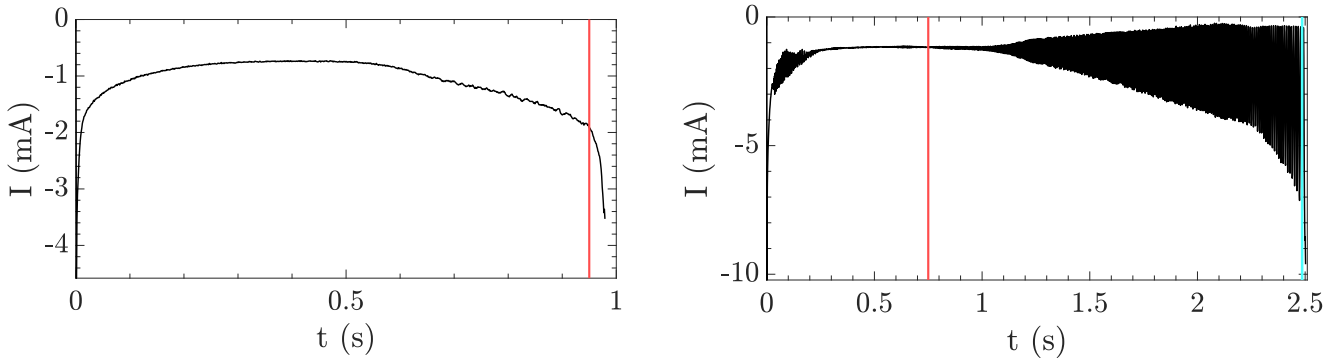

(a) $\phi_c = -3$ V (b) $\phi_c = -7$ V

FIG. 5: Transient behavior of the cell current during one bubble evolution cycle at (a) $\phi_c = -3$ V and (b) $\phi_c = -7$ V electrode potential for $c = 0.5$ M H_2SO_4 solution. The red lines correspond to the parameters given in Table II; the blue line corresponds to FIG. 3a

At time instants when the bubble is steadily growing on the electrode carpet and not undergoing additional motion, the bubble is in a state of equilibrium of forces. If the instant is in the later part of the growth cycle, the growth rate is small enough that history effects (F_{hs}) can be safely neglected. Thus, under the assumption of a uniform interfacial charge density (σ), Eq. 16 gives us

$$\sigma = -\frac{F_b + F_h}{f_e} \tag{20}$$

where, $f_e = \int E dA$. Now we choose two instants of force equilibrium when the bubble is not oscillating as shown in FIG. 5, namely,

(a) a time instant just before detachment for a scenario when the bubble is not oscillating at all, henceforth referred to as non-oscillating

(b) a time instant before the bubble starts to oscillate, henceforth referred to as pre-oscillating

The parameters used in the simulations are given in Table II and Appendix A. For the remaining small difference in the current values in case (b) we also refer to the discussion in subsection B. The force components and the surface charge density obtained from the simulations are shown in Table III. The surface charge density, given in the rightmost column, is calculated using Eq. 20. The two values are close to each other and are furthermore in good agreement with the value of $\sigma = 1.98$ mC/m^2 reported earlier by Bashkatov et al. [9] without the model improvements considered in this work.

Case	ϕ_c (V)	D_b (μm)	δ (μm)	ϵ (μm)	Θ	I_{exp} (mA)	I_{sim} (mA)
(a)	-3	634	9	6	84.6	2	2
(b)	-7	645	1	7	99.6	1.17	1.25

TABLE II: Simulation parameters for non- & pre-oscillating cases: ϕ_c, D_b, δ, ε and I_{exp} as obtained by measurement, Θ is a model parameter and obtained by properly adjusting the cell current I_{sim}

Case	F_M (μN)	F_p (μN)	F_v (μN)	F_h (μN)	F_b (μN)	f_e (Vm)	σ (mC/m^2)
(a)	-0.21	-0.43	-0.16	-0.59	1.31	-3.3e-4	2.18
(b)	-0.17	-0.5	-0.14	-0.64	1.38	-3.38e-4	2.19

TABLE III: Simulation results of forces and surface charge density for non- and pre-oscillating cases

B. Oscillating bubble

1. *Correlation of simulations with measurements*

Position	D_b (μm)	δ (μm)	ϵ (μm)	Θ	I_{exp} (mA)	$I_{sim}(mA)$
Lowest	985	0	13.21	99.92	0.3	0.9
Highest	985	14.35	33.04	54.76	7	7.00

TABLE IV: Simulation parameters and experimental data near the time instant marked blue in FIG. 5b. $\phi_c = -7$ V.

Now we look in detail at the oscillatory bubble behavior close to departure. Table IV shows the experimental and simulation data near the time instant marked blue in FIG. 5b for the lowest and the highest bubble positions. Further details on the choice of the potential $\Delta\Phi_{sim}$ and the gas coverage Θ in the oscillatory regime are given in Appendix A. As can be seen, at the highest bubble position, a perfect match of the cell current in experiment and simulation is obtained by adjusting the carpet size in the simulations to $\Theta = 54.76$. However, at the lowest bubble position, there is still a small difference in the electric current values. Here, even when the gas coverage of the electrode is close to 100, the cell current in the simulation is still stronger than in the experiment. This is due to the fact that, as mentioned in Section III A, the nature of the gas carpet is not uniformly insulating as assumed in the model. Hence, electric current can pass through films of electrolyte between the small bubbles that constitute the carpet, increasing the resistance to the current while the gas coverage (Θ) of the electrode remains the same. This leads to a smaller current in the experiment compared to the simulation even when $\Theta > 99$.

2. *Electrolyte velocities in the vicinity of an oscillating bubble*

FIGs. 6a and 6b show the flow velocity measured by μPTV near the lower half of the bubble at the top and bottom positions during one cycle of oscillation. FIGs. 6c and 6d show the flow velocity obtained from simulations. It can be seen that the calculated flow velocities are in qualitative agreement with the measured velocities. At first sight, the electrolyte flow at both bubble positions is in good qualitative agreement with the flow measurements in the stationary bubble regime performed by Massing et al. [12]. As can be further seen, the interfacial flow is stronger at the highest bubble position (FIG. 6a) than at the lowest position (FIG. 6)). This correlates well with the higher current at the top position (see FIG. 2) due to a lower ohmic resistance, which then causes a stronger thermocapillary

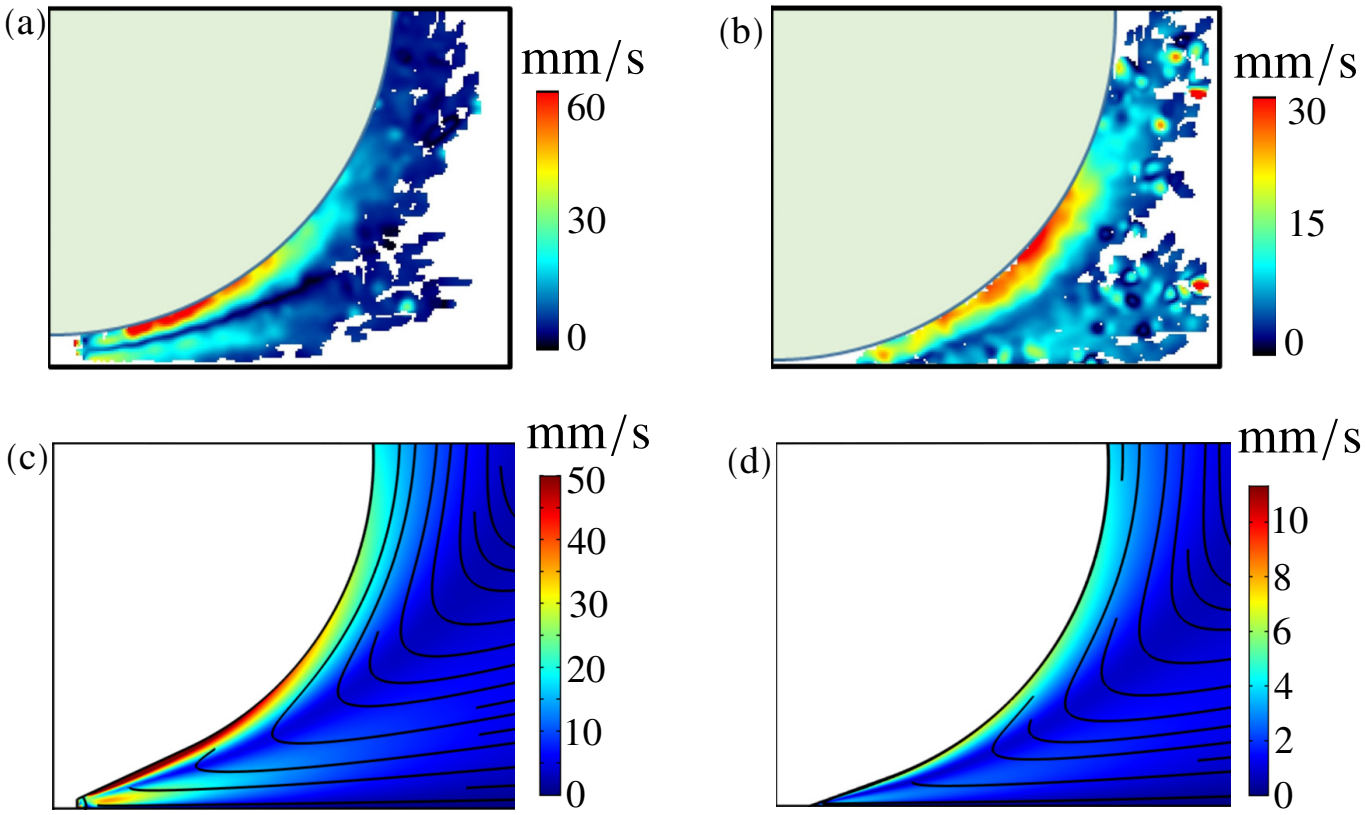

FIG. 6: Flow velocity as obtained from μPTV measurements (top) and simulations (bottom) in the highest position (left) and the lowest position (right) of the bubble oscillation during one cycle. Please note the different velocity scales.

effect. As the thermocapillary effect decreases at the bottom position, the flow velocity is lower. The proximity of the bottom wall during the lower half of the oscillation may also be expected to exert a stronger damping effect on the electrolyte flow in general.

Next, we discuss the flow velocity profiles at the interface and to draw a more detailed comparison between the simulations and measurements. The simulations were carried out for one oscillation cycle and for the experimental and simulation parameters given in Table IV. FIG. 7 shows the velocity profiles at the topmost (a) and the bottommost position (b) of the bubble as a function of angular position (θ). The experimental profiles shown in FIG. 7 are extracted from FIGs. 6a and 6b. Because of the finite size of the tracer particles, the simulation results are shown at different distances from the bubble interface [12].

In general, the nature of the velocity profiles is similar to previous findings [12–14]. It can be seen in FIG. 7 that the predicted velocity compares well with the measurement at the upper oscillation position, whereas significant deviations occur at the bottom position. At the upper bubble position, the low gas coverage of the electrode, along with the large δ and ε, causes a comparably low electrical resistance, which is then evident in a high cell current. This causes considerable Joule heating and, in turn, steep interfacial temperature gradients, leading to a strong thermocapillary flow of about 70 mm/s near the bubble foot. As can be seen in FIG. 7a, this phenomenon is captured well in the simulation. Similarly to Massing et al., an almost perfect match between the peak velocity and the peak angle is obtained for the simulated profile at 5 μm, which corresponds well with the size of the tracer particles [12]. At larger angles of $\theta > 40°$, the measured velocity amplitude seems to decrease faster than the velocity simulated. This difference could be due to unaccounted-for solutocapillary effects present in the experiment, as hypothesized by Meulenbroek et al. [14]. However, we would also like to note at this juncture that the presence of the particles added to the electrolyte to perform the PTV experiments may also alter the behavior of the interface. It is likely that these particles reduce the mobility of the interface, which points to the same qualitative difference seen between the measurements and calculations. As the bubble moves down, the cell current decreases and thus the driving force of the thermocapillary flow. Indeed, for the quasi-stationary simulation at the low position of the bubble, the predicted amplitude of the thermocapillary flow is very weak, as seen in FIG. 7b. However, as the bubble rapidly sinks during its fast oscillatory motion, though the cell current and thus the heating decrease immediately, the thermocapillary

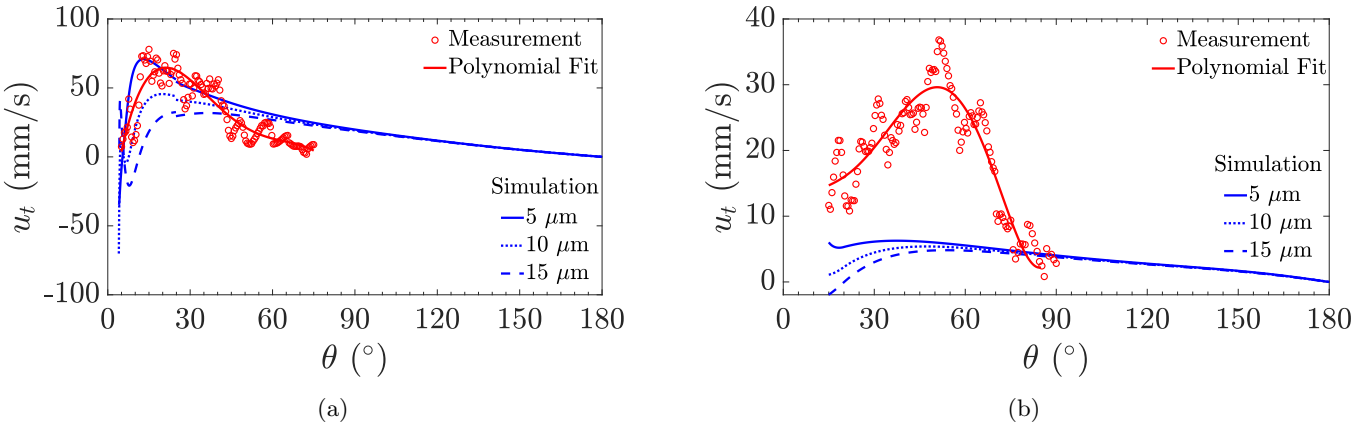

FIG. 7: Comparison of the flow velocities between simulation and measurement at (a) highest position and (b) lowest position of the bubble oscillation during one cycle. The simulation results are shown at various distances from the bubble interface, indicated by blue lines. The red symbols capture the measurement points from μPTV and the red line represents the polynomial fit. The angular position θ is defined in FIG. 3b.

flow from the top position has not yet completely decayed (see the time scales shown in Table I). Thus, a residual flow is also captured in the measurement. The amplitude of the interfacial flow measured is about half the amplitude measured at the top position. Thus, the difference between the numerical prediction and measurement seen in FIG. 7b originates from the fast timescale of the bubble oscillation, which is not completely taken into account considering the quasi-stationary nature of our simulation approach. A further difference appears with respect to the angular position at which the velocity is at a maximum. Compared to the top position of the bubble, the maximum at the low position appears at larger angles, in both the measurement and simulation. Moreover, this angle is now larger in the measurement than in the simulations (5 μm). This points to the conclusion that this shift in the maximum angle is caused partially by the geometric changes between the bottom and top positions of the bubble, as can be seen in the simulation result, and mainly by the decaying thermocapillary flow originating from the top position, which continues to move electrolyte upwards as the bubble moves down.

3. *Quantification of forces*

In this section, we discuss the forces acting on the bubble during one oscillation cycle. We start by obtaining an approximation for the history force. As the bubble deformation is small ($\varepsilon \ll R_b$), we use the expression for a sphere given by [50],

$$F_{hs} = -6R_b^2\sqrt{\pi\rho\mu}\int_0^t \frac{\dot{U}(s)\mathrm{d}s}{\sqrt{t-s}} \tag{21}$$

Based on a harmonic bubble oscillation given by $U(t) = U_0\sin(\omega t)$, we also derive a simplified expression. Further details of the derivation for the history force are given in Appendix B. To quantify the history force, the values of the parameters used in the calculation are: $U_0 = 1$ mm/s, $\omega = 200\pi$, $R_b = 0.5$ mm, $\rho = 1000$ kg/m^3, $\mu = 8.9\times10^{-4}$ Pa·s. The force values obtained during about three bubble oscillations are shown in FIG. 8, superimposed with the bubble velocity U. As can be seen, the history force oscillates with the same frequency as the bubble does, with maxima and minima slightly ahead in time of the bubble velocity. The magnitude of the history force amounts to about 0.1 μ N only and hence is much smaller than the buoyancy force (see FIG. 9d). Thus, the influence of the history force due to position oscillations of the bubble is neglected in the following, and the force balance, Eq. 16, becomes

$$F_b + F_h + F_e = 0 \tag{22}$$

Now, we focus on quantifying the hydrodynamic (F_h) and the electric force (F_e) during the bubble oscillations. For this, one oscillation cycle just before the detachment of the bubble is depicted. At seven instants of time within this cycle, simulations as described in Section III A are performed based on the geometric and current parameters obtained from experimental data. FIG. 9(a) shows the 7 consecutive frames of bubble images captured during the experiment using high speed shadowgraphy. With the help of the horizontal red line guiding the eyes, it can be seen

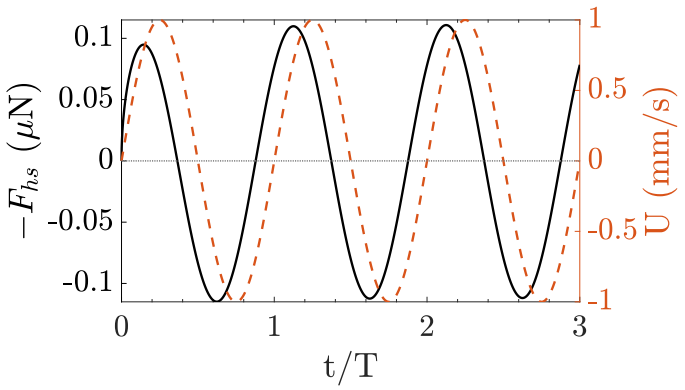

FIG. 8: Temporal behavior of the history force and the bubble velocity in the oscillatory mode.

that the bubble undergoes position oscillations. One full cycle is shown. The bubble diameter is 985 μm. The right- and leftmost frames depict the bubble at the highest position, while the middle frame shows the bubble at the lowest position. FIG. 9(b) shows the cell currents obtained from the simulation of each case (I_{sim}) along with the cell current measured (I_{exp}) during the experiment. In FIG. 9(c), the carpet thickness (δ) and the bubble elongation (ε) along with the values of Θ used in each simulation are shown at each of the chosen instants.

From FIGs. 9(a), (b) and (c), it can be seen that as the bubble undergoes the position oscillation, the associated physical parameters vary periodically in time during one cycle. Around the highest position of the bubble, δ and ε attain their maximum values. We also see that the cell current is largest at the highest position obtained in the experiment by a small electrode gas coverage (Θ). During the course of the oscillation cycle, as the bubble moves down, δ and ε decrease and Θ increases. The cell current also drops as the resistance to electric current increases at the bottom position. This trend is then reversed as the bubble starts to move upward again.

FIG. 9(d) shows the variation in the hydrodynamic force (F_h), Marangoni force (F_M) and electric force (F_e) as obtained from the simulation, along with the buoyancy force (F_b) acting upward. Since an estimation of the interfacial charge density (σ) is required to calculate F_e, one further calculation was carried out at the instant of bubble detachment, marked with a purple cross at t=2.337 s in the $I_{exp}(t)$ curve in FIG. 9. The parameters used in the simulation are as follows: $D_b = 2R_b = 985$ μm, $\delta = 18.17$ μm, $\varepsilon = 32.83$ μm, $I_{exp} = -7.51$ mA, $I_{sim} = -7.4$ mA, $\Theta = 54.76$. We then use Eq. 20 to calculate the surface charge density and obtain $\sigma = 2.07$ mC/m^2, which is in good correlation with the value we obtained for a stationary bubble in Section IV A. This value is then used in the F_e calculation plotted in the bottom panel of FIG. 9.

Since the bubble does not grow much during the one oscillation period considered, the upward acting buoyancy force F_b remains nearly constant. In contrast, F_M, F_h and F_e are acting downward and vary during the oscillation cycle. Since F_M is part of F_h, $F_M < F_h$. The downward forces act as a restoring mechanism against the departing action of buoyancy and lead to the oscillatory mode of the bubble dynamics. According to Eq. (14),

$$F_T = F_h + F_e + F_b \tag{23}$$

is the total force acting on the bubble, which is also plotted in FIG. 9(d) alongside all the other forces. The action of the electric force F_e as an important part of the force balance was first introduced by Bashkatov et al. [9] to explain the observed position oscillations and to obtain good correlation between the model prediction and observation in terms of oscillation frequency and amplitude. Since the effect of flow physics on the oscillatory dynamics was left for future study by Ref [9], the temporal behavior of F_T shown in FIG. 9(d) captures a first approximation of such effects. As can be seen, the total force F_T periodically changes its sign, which is in line with the position oscillations observed, but the magnitudes of F_T near the bottom position are much greater than near the top position of the bubble. It appears likely that this is at least partly caused by the underestimation of the Marangoni force F_M and consequently the hydrodynamic force F_h in the lower bubble positions. As already discussed in Section IV B 1, and as can be seen in FIG. 7b, the magnitude of the electrolyte flow during the bottom half of the bubble oscillation is not fully captured by the simulations conducted at fixed bubble positions. Thus, we overestimate F_T in the lower half of the position oscillation, which may contribute to the observed behavior of F_T. Further asymmetric contributions may result from the top-bottom asymmetry in the geometry, as seen from the temporal behavior of e.g. the bubble deformation ε during the oscillation and possible additional details from non-linear dynamics. To examine the correlation of the total force and the bubble motion in detail, at t= 2.32 s, the bubble is at the lowest position and the total force as calculated reaches a maximum in the upward direction, which causes the bubble to move up. Eventually, the bubble

attains force equilibrium at 2.322 s $< t <$ 2.324 s. Then the bubble decelerates as F_T becomes negative, and comes to a stop at 2.326 s. $F_T = -0.025$ μN in the highest position. A similar (mirror image) trend is also expected in the left half of the $F_T(t)$ curve where the bubble moves downward. As $F_T = -0.006$ μN at t=2.314 s, the F_T curve crosses the zero line immediately after the zero line, though this is not clearly visible in FIG. 9. Even though our model contains simplifying assumptions which do not fully account for rapid transient effects, the calculated temporal behavior of total force provides a good qualitative correlation with the observed oscillatory bubble motion.

V. CONCLUSION

The present work provides a detailed investigation of the complex dynamics of hydrogen bubbles growing above a carpet of microbubbles at a microelectrode. The focus of the work is on gaining an improved understanding on the oscillatory bubble behavior prior to departure that occurs at strongly negative electrode potentials in an acidic electrolyte. Compared to earlier work [9], this is achieved by analyzing the full set of relevant forces quantitatively, which are the buoyancy force, the electric force and the hydrodynamic force caused by the thermocapillary effect. Besides, the minor influence of history force effects and the bubble-carpet interaction is discussed. The numerical simulations of the bubble dynamics performed now resemble the geometric aspects and experimental conditions in more detail than before [9]. They account for the bubble deformation, and, in order to match the cell current measured in the experiments, the cell voltage and the degree of gas coverage of the electrode are now adjusted accordingly. This clearly advances the overall accuracy of the simulations and allows a detailed quantitative analysis of the bubble forces acting during the oscillations. Besides, further support to an improved understanding is given by PTV velocity data that characterize the electrolyte flow pattern at time instants during the fast lateral bubble oscillation. These were obtained by phase averaging over a number of oscillation cycles.

In situations the bubble is nearly resting, the force balance can be used to estimate the electric charge density of the bubble. We found that the results of the simulations for a bubble either shortly before the lift-off in stationary mode or shortly before the onset of oscillations deliver values close by ($\sigma = 2.1 \pm 0.1$ C/m^2), which interestingly also nicely match with the value obtained in earlier research [9]. This clearly gives strong support for the role of the electric force in the dynamics of electrolytic bubbles that has been considered only little so far. Whether the charge density is indeed spatially constant along the bubble surface that is exposed to a strongly inhomogeneous electric field nearby the micro-electrode can not be answered by this work. In that sense, the value of σ might more safely be considered as a mean charge density.

When analyzing the oscillatory regime, it is found that the full set of forces considered delivers a total force on the bubble that is oscillating with time accordingly. This confirms that the oscillatory motion is enabled by the electrode-distance-varying amplitude of the electric and the hydrodynamic forces that act downward against buoyancy.

We have to admit that the results of the numerical analysis performed may partly be influenced by the remaining approximations of the simulation model. As can be seen from the comparison of the interfacial velocity profiles during the bubble oscillation from measurement and simulation (see Fig. 7), the thermocapillary motion of the bubble interface is underestimated in the simulations at lower points of the bubble position. This is due to the fact that the quasisteady approach we take in the simulations can not account for inertial parts of the interfacial motion that are still visible here due to the fast oscillatory bubble dynamics at about 100 Hz. In future research, it would be therefore useful to directly take into account the vertical bubble motion, e.g. by using a moving mesh method. We have further to admit that the procedure of picking a proper couple of potential and carpet size values leaves some level of ambiguity. It would be therefore desirable to perform future experiments that deliver data of the temporal evolution of the geometry and also the inner structure of the carpet of microbubbles at higher resolution, which would allow for a further improved simulation model. Finally, the interesting question how the experimental conditions, e.g. potential and acid concentration, influence the arising of the different bubble growth modes will be addressed in a future work [44].

ACKNOWLEDGEMENT

This work was supported by the German Aerospace Center (DLR) with funds provided by the Federal Ministry for Economic Affairs and Energy (BMWi) due to an enactment of the German Bundestag under grant no. DLR 50WM2058 (MADAGAS II project).

APPENDIX

A. Choice of $\Delta\phi_{sim}$ and Θ

Here we discuss the choices of Θ in conjunction with the potential difference between the cathode and anode ($\Delta\phi_{sim}$) applied in the simulation. The values of the ($\Delta\phi_{sim}$,Θ) pair for the simulation results presented in this study are given in Table V.

Case	ϕ_c (V)	$\Delta\phi_{sim}$ (V)	Θ
FIG. 5a	-3	2.5	84.6
FIG. 5b	-7	3	99.6
FIG. 7a	-7	4.5	54.76
FIG. 7b	-7	4.5	99.92
FIG. 9	-7	4.5	Varied - cf. FIG. 9(c)

TABLE V: Values of $\Delta\phi_{sim}$ and Θ for different simulation cases at two cathode potentials ϕ_c.

We start with the case shown in FIG. 7b. As we expect almost full gas coverage of the electrode at the low oscillation position, a large value of Θ is chosen. Then, $\Delta\phi_{sim}$ is applied such that a close match between the I_{sim} and I_{exp} can be obtained. This same value of $\Delta\phi$ is then applied for the case of FIG. 7a and the different instances of FIG. 9, and Θ is adjusted to obtain a good correlation between the calculated and measured cell currents. For FIG. 5b a similar method is applied, but since the time instant is different, i.e., the cell current and the bubble size are different, a different value of $\Delta\phi$ is obtained when the gas coverage of the cathode is almost full.

Next, we discuss the ($\Delta\phi_{sim}$,Θ) pair for FIG. 5a. Since $\Delta\phi_{sim}$ and Θ jointly determine I_{sim}, in this case it is possible to choose different pairs that give the same cell current. Though the result for one particular set of ($\Delta\phi_{sim}$,Θ) pairs is given in Section IV A, in Table VI we show the calculated surface charge density (σ) values at various ($\Delta\phi_{sim}$,Θ) pair values producing a good match between I_{sim} and I_{exp}. The results of row #b in Table VI are shown in Section IV A. At values of Θ which are less than the value given in Table VI row #a, the gas coverage is too low to be physically realistic, whereas Table VI row #c captures the upper limit, since $\Theta < 100$. Thus, within the limits of the model, the range of σ estimation lies within 1.52 – 2.3 mC/m^2; this correlates well with the range of experimental measurements reported in the literature [9].

#	$\Delta\phi_{sim}$ (V)	Θ	I_{sim} (mA)	I_{exp} (mA)	σ (mC/m^2)
a	2.4	54.76	2.09	2	2.30
b	2.5	84.6	2.01	2	2.18
c	3	98.8	2.08	2	1.52

TABLE VI: Various combinations of ($\Delta\phi$,Θ) pairs for FIG. 5a.

Next, we discuss the cell voltage from an electrochemical standpoint and how it relates to the potential difference between the cathode and anode applied in the simulation, namely $\Delta\phi_{sim}$. The cell voltage, as defined electrochemically, is obtained as the difference in electric potential between the anode and the cathode and is given by [56],

$$V = \eta_{s,anode} + \eta_{c,anode} + U_{eq} + \Delta\Phi_{ohm} - \eta_{s,cathode} - \eta_{c,cathode} \tag{24}$$

Here, V is the cell voltage, η_s is the surface overpotential and η_c is the concentration overpotential at the electrodes, U_{eq} is the equilibrium potential and $\Delta\Phi_{ohm}$ is the potential drop due to Ohmic resistance. In our current model, we neglect the effects of overpotential at the electrode-electrolyte junction, thus $\Delta\phi_{sim}$ attempts to capture the contribution $U_{eq} + \Delta\Phi_{ohm}$ in Eq. 24. $U_{eq} = 1.23$ V, from the thermodynamics of the electrochemical reaction [57]; as a result, the potential distribution in the cell as determined in the simulation (ϕ) deals with the Ohmic losses.

In the electrochemical cell, the Ohmic resistance to the cell current has multiple contributions, namely, the large H_2 bubble growing on the Pt microelectrode or the cathode, the collection of smaller bubbles that covers the cathode, the O_2 bubbles covering the anode and, finally, the resistance provided by the electrolyte. However, the largest contribution to the total cell resistance comes from the H_2 bubble. Thus it can be written that

$$\Delta\Phi_{ohm} = \Delta\Phi_{H_2} + \Delta\Phi_{carpet} + \Delta\Phi_{electrolyte} + \Delta\Phi_{O_2} \tag{25}$$

In the model, the geometric features of the large H_2 bubble (R_b and ε) are taken from the experiment. The resistance provided by the bubble ($\Delta\Phi_{H_2}$) is therefore captured well in the model. The thickness of the carpet layer (δ) is also measurable in experiment and is fed into the model. Since it is not possible to directly resolve the gas coverage of the cathode (R_g in FIG. 3b) accurately in the experiment, the R_g value chosen and thus Θ represent a model parameter which in turn determines the value of $\Delta\Phi_{carpet}$ captured by the model. As the current path in the simulation does not exactly mimic the placement of the anode in the experiment, we expect a difference in the $\Delta\Phi_{electrolyte}$ between the model and experiment. Lastly, $\Delta\Phi_{O_2}$ is not present in the simulation since we ignore the O_2 bubbles in the model. Accordingly, the cell voltage that can be measured during an electrochemical experiment and the difference in potential between the cathode and the anode that is applied in the model are not exactly the same. Since the current distribution around the H_2 bubble is the major determining factor for the interfacial phenomena for an electrolytic bubble growing on a microelectrode [12], we match the cell current with the knowledge that the resistance to the cell current close to the cathode is captured well in the model.

B. Calculation of history force

Let us assume that the particle is executing a simple harmonic motion given by $U(t) = U_0 \sin(\omega t)$. We now want to evaluate the integral contained in the history force,

$$\mathcal{I} = \int_0^t \frac{\dot{U}(s)\,\mathrm{d}s}{\sqrt{t-s}} \tag{26}$$

Substituting the expression for particle velocity,

$$\mathcal{I} = U_0\omega \int_0^t \frac{\cos(\omega s)}{\sqrt{t-s}}\,\mathrm{d}s \tag{27}$$

Let us say that $t - s = x^2$. Substituting in the above, we obtain

$$\mathcal{I}_0 = 2\sin(\omega t)\int_0^{\sqrt{t}} \sin(\omega x^2)\,\mathrm{d}x + 2\cos(\omega t)\int_0^{\sqrt{t}} \cos(\omega x^2)\,\mathrm{d}x \tag{28}$$

where $\mathcal{I}_0 = \int_0^t \frac{\cos(\omega s)}{\sqrt{t-s}}\,\mathrm{d}s$. Now, we perform one more variable transformation, namely $\omega x^2 = \pi/2y^2$ and get

$$\mathcal{I}_0 = \sqrt{\frac{2\pi}{\omega}}\left[2\sin(\omega t)\int_0^{\sqrt{\frac{2\omega t}{\pi}}} \sin\left(\frac{\pi y^2}{2}\right)\mathrm{d}y + 2\cos(\omega t)\int_0^{\sqrt{\frac{2\omega t}{\pi}}} \cos\left(\frac{\pi y^2}{2}\right)\mathrm{d}y\right] \tag{29}$$

Here, we make use of Fresnel integrals, defined as $\mathcal{F}_c(\tau) = \int_0^\tau \cos\left(\frac{\pi z^2}{2}\right)\mathrm{d}z$ and $\mathcal{F}_s(\tau) = \int_0^\tau \sin\left(\frac{\pi z^2}{2}\right)\mathrm{d}z$ and thus we obtain the history force acting on an oscillating particle at time t as

$$F_{hs}(t) = -6\pi U_0 R_b^2\sqrt{2\rho\mu\omega}\left[\sin(\omega t)\,\mathcal{F}_s\left(\sqrt{\frac{2\omega t}{\pi}}\right) + \cos(\omega t)\,\mathcal{F}_c\left(\sqrt{\frac{2\omega t}{\pi}}\right)\right] \tag{30}$$

C. Material properties

Properties of the electrolyte, as used in the simulations, are given in Table VII. The properties of other materials are given in Table VIII.

[1] Federal Ministry for Economic Affairs and Energy. The national hydrogen strategy. `https://www.bmwi.de/Redaktion/EN/Publikationen/Energie/the-national-hydrogen-strategy.html` (accessed on 2021-05-05).

[2] European Commission. A european green deal. `https://ec.europa.eu/info/strategy/priorities-2019-2024/european-green-deal_en` (accessed on 2021-05-05).

[3] Ankica Kovač, Matej Paranos, and Doria Marciuš. Hydrogen in energy transition: A review. *International Journal of Hydrogen Energy*, 46:10016, 2021.

μ	10^{-3}	Pa·s
σ_e	20	S/m
ρ	10^3	kg/m^3
C_p	4.182	kJ/kg·K
k	0.58	W/m·K
β	-1.6×10^{-4}	N/(m·K)

TABLE VII: Properties of the electrolyte and the interface used in the simulations.

Material	ρ(kg/m^3)	C_p(kJ/kg·K)	k(W/m·K)
Platinum	21450	0.13	72
Glass	2201	1.052	1.38
Hydrogen	0.09	14.32	0.186

TABLE VIII: Material properties of the electrodes, the glass cuvette and the gas bubble.

[4] S Shiva Kumar and V Himabindu. Hydrogen production by PEM water electrolysis–a review. *Materials Science for Energy Technologies*, 2(3):442–454, 2019.

[5] Wenming Tong, Mark Forster, Fabio Dionigi, Sören Dresp, Roghayeh Sadeghi Erami, Peter Strasser, Alexander J Cowan, and Pau Farràs. Electrolysis of low-grade and saline surface water. *Nature Energy*, 5(5):367–377, 2020.

[6] Daniel Siegmund, Sebastian Metz, Volker Peinecke, Terence E Warner, Carsten Cremers, Anna Grevé, Tom Smolinka, Doris Segets, and Ulf-Peter Apfel. Crossing the valley of death: From fundamental to applied research in electrolysis. *JACS Au*, 1(5):527–535, 2021.

[7] SA Grigoriev, VN Fateev, DG Bessarabov, and P Millet. Current status, research trends, and challenges in water electrolysis science and technology. *International Journal of Hydrogen Energy*, 45(49):26036–26058, 2020.

[8] GE Thorncroft and James F Klausner. Bubble forces and detachment models. *Multiphase Science and Technology*, 13(3&4), 2001.

[9] Aleksandr Bashkatov, Syed Sahil Hossain, Xuegeng Yang, Gerd Mutschke, and Kerstin Eckert. Oscillating hydrogen bubbles at Pt microelectrodes. *Physical Review Letters*, 123:214503, 2019.

[10] Xiaowei Hu, Zhenshan Cao, Yechun Wang, Shaohua Shen, Liejin Guo, and Juanwen Chen. Single photogenerated bubble at gas-evolving TiO_2 nanorod-array electrode. *Electrochimica Acta*, 202:175–185, 2016.

[11] Xuegeng Yang, Dominik Baczyzmalski, Christian Cierpka, Gerd Mutschke, and Kerstin Eckert. Marangoni convection at electrogenerated hydrogen bubbles. *Physical Chemistry Chemical Physics*, 20(17):11542–11548, 2018.

[12] Julian Massing, Gerd Mutschke, Dominik Baczyzmalski, Syed Sahil Hossain, Xuegeng Yang, Kerstin Eckert, and Christian Cierpka. Thermocapillary convection during hydrogen evolution at microelectrodes. *Electrochimica Acta*, 297:929–940, 2019.

[13] Syed Sahil Hossain, Gerd Mutschke, Aleksandr Bashkatov, and Kerstin Eckert. The thermocapillary effect on gas bubbles growing on electrodes of different sizes. *Electrochimica Acta*, 353:136461, 2020.

[14] AM Meulenbroek, AW Vreman, and NG Deen. Competing marangoni effects form a stagnant cap on the interface of a hydrogen bubble attached to a microelectrode. *Electrochimica Acta*, 385:138298, 2021.

[15] Nakul Pande, Jeffery A Wood, Guido Mul, Detlef Lohse, Bastian T Mei, and Dominik Krug. Electroconvective instability in water electrolysis: an evaluation of electroconvective patterns and their onset features. *arXiv preprint arXiv:2101.08542*, 2021.

[16] Xiaowei Hu, Meng Sun, Jugan Zheng, and Heqing Jiang. The thermal Marangoni effect during photoelectrochemical conversion. In *IOP Conference Series: Earth and Environmental Science*, volume 675, page 012187. IOP Publishing, 2021.

[17] L Gary Leal. *Advanced Transport Phenomena: Fluid Mechanics and Convective Transport Processes*, volume 7. Cambridge University Press, 2007.

[18] NO Young, Jo S Goldstein, and Mi J Block. The motion of bubbles in a vertical temperature gradient. *Journal of Fluid Mechanics*, 6(3):350–356, 1959.

[19] Bert K Larkin. Thermocapillary flow around hemispherical bubble. *AIChE Journal*, 16(1):101–107, 1970.

[20] YS Kao and DBR Kenning. Thermocapillary flow near a hemispherical bubble on a heated wall. *Journal of Fluid Mechanics*, 53(4):715–735, 1972.

[21] M Kassemi and N Rashidnia. Steady and oscillatory thermocapillary convection generated by a bubble. *Physics of Fluids*, 12(12):3133–3146, 2000.

[22] Steven Lubetkin. Thermal marangoni effects on gas bubbles are generally accompanied by solutal marangoni effects. *Langmuir*, 19(26):10774–10778, 2003.

[23] Scott A Guelcher, Yuri E Solomentsev, Paul J Sides, and John L Anderson. Thermocapillary phenomena and bubble coalescence during electrolytic gas evolution. *Journal of the Electrochemical Society*, 145(6):1848, 1998.

[24] Paul J Sides and Charles W Tobias. A close view of gas evolution from the back side of a transparent electrode. *Journal of the Electrochemical Society*, 132(3):583, 1985.

[25] SD Lubetkin. The fundamentals of bubble evolution. *Chemical Society Reviews*, 24(4):243–250, 1995.

[26] Steven Lubetkin. The motion of electrolytic gas bubbles near electrodes. *Electrochimica Acta*, 48(4):357–375, 2002.

[27] G Quincke. Über die fortführung materieller Theilchen durch strömende Elektricität. *Annalen der Physik*, 189(8):513–598, 1861.

[28] H.A. McTaggart. XXXIII. The electrification at liquid-gas surfaces. *The London, Edinburgh, and Dublin Philosophical Magazine and Journal of Science*, 27(158):297–314, 1914.

[29] Thomas Alty. The cataphoresis of gas bubbles in water. *Proceedings of the Royal Society of London. Series A*, 106(737):315–340, 1924.

[30] Masayoshi Takahashi. ζ potential of microbubbles in aqueous solutions: electrical properties of the gas- water interface. *The Journal of Physical Chemistry B*, 109(46):21858–21864, 2005.

[31] Chun Yang, Tadeusz Dabros, Dongqing Li, Jan Czarnecki, and Jacob H Masliyah. Measurement of the zeta potential of gas bubbles in aqueous solutions by microelectrophoresis method. *Journal of Colloid and Interface Science*, 243(1):128–135, 2001.

[32] Jong-Yun Kim, Myung-Geun Song, and Jong-Duk Kim. Zeta potential of nanobubbles generated by ultrasonication in aqueous alkyl polyglycoside solutions. *Journal of colloid and interface science*, 223(2):285–291, 2000.

[33] Aphirak Phianmongkhol and Julie Varley. ζ potential measurement for air bubbles in protein solutions. *Journal of colloid and interface science*, 260(2):332–338, 2003.

[34] NP Brandon, GH Kelsall, S Levine, and AL Smith. Interfacial electrical properties of electrogenerated bubbles. *Journal of Applied Electrochemistry*, 15(4):485–493, 1985.

[35] Donald Eugene Westerheide and JW Westwater. Isothermal growth of hydrogen bubbles during electrolysis. *AIChE Journal*, 7(3):357–362, 1961.

[36] Geoffrey H Kelsall, Shanyu Tang, Saruhan Yurdakul, and Alec L Smith. Electrophoretic behaviour of bubbles in aqueous electrolytes. *Journal of the Chemical Society, Faraday Transactions*, 92(20):3887–3893, 1996.

[37] Geoffrey H Kelsall, Shanyu Tang, Alec L Smith, and Saruhan Yurdakul. Measurement of rise and electrophoretic velocities of gas bubbles. *Journal of the Chemical Society, Faraday Transactions*, 92(20):3879–3885, 1996.

[38] RS Schechter, A Graciaa, and J Lachaise. The electrical state of a gas/water interface. *Journal of Colloid and Interface Science*, 204(2):398–399, 1998.

[39] Ángel V Delgado. *Interfacial Electrokinetics and Electrophoresis*, volume 106. CRC Press, 2001.

[40] Christine L Henry, Luke Parkinson, John R Ralston, and Vincent SJ Craig. A mobile gas- water interface in electrolyte solutions. *The Journal of Physical Chemistry C*, 112(39):15094–15097, 2008.

[41] Patrice Creux, Jean Lachaise, Alain Graciaa, James K Beattie, and Alex M Djerdjev. Strong specific hydroxide ion binding at the pristine oil/water and air/water interfaces. *The Journal of Physical Chemistry B*, 113(43):14146–14150, 2009.

[42] Brian J Kirby. *Micro-and Nanoscale Fluid Mechanics: Transport in Microfluidic Devices*. Cambridge university press, 2010.

[43] Peter K. Weissenborn and Robert J. Pugh. Surface tension of aqueous solutions of electrolytes: relationship with ion hydration, oxygen solubility, and bubble coalescence. *Journal of Colloid and Interface Science*, 184(2):550–563, 1996.

[44] Aleksandr Bashkatov, Syed Sahil Hossain, Xuegeng Yang, Hannes Rox, Inez Weidinger, Gerd Mutschke, and Kerstin Eckert. On the growth regimes of hydrogen bubbles at microelectrodes. submitted to Phys. Chem. Chem. Phys.

[45] Géraldine Duhar and Catherine Colin. Dynamics of bubble growth and detachment in a viscous shear flow. *Physics of Fluids*, 18(7):077101, 2006.

[46] Jacob N Israelachvili. *Intermolecular and Surface Forces*. Academic press, 2015.

[47] Hans-Jürgen Butt and Michael Kappl. *Surface and Interfacial Forces*. John Wiley & Sons, 2018.

[48] Jacques Magnaudet and Dominique Legendre. The viscous drag force on a spherical bubble with a time-dependent radius. *Physics of Fluids*, 10(3):550–554, 1998.

[49] Aleksandr Bashkatov, Xuegeng Yang, Gerd Mutschke, Barbara Fritzsche, Syed Sahil Hossain, and Kerstin Eckert. Dynamics of single hydrogen bubbles at Pt microelectrodes in microgravity. *Phys. Chem. Chem. Phys.*, 23:11818–11830, 2021.

[50] Roland Clift, John R Grace, and Martin E Weber. *Bubbles, drops, and particles*. Courier Corporation, 2005.

[51] CE Brennen. A review of added mass and fluid inertial forces. Technical report, Naval Civil Engineering Laboratory, Port Hueneme, California, 1982.

[52] WC Park, JF Klausner, and R Mei. Unsteady forces on spherical bubbles. *Experiments in fluids*, 19(3):167–172, 1995.

[53] M Abbad and M Souhar. Experimental investigation on the history force acting on oscillating fluid spheres at low reynolds number. *Physics of Fluids*, 16(10):3808–3817, 2004.

[54] MAT Van Hinsberg, JHM ten Thije Boonkkamp, and Hans JH Clercx. An efficient, second order method for the approximation of the basset history force. *Journal of Computational Physics*, 230(4):1465–1478, 2011.

[55] Xuegeng Yang, Franziska Karnbach, Margitta Uhlemann, Stefan Odenbach, and Kerstin Eckert. Dynamics of single hydrogen bubbles at a platinum microelectrode. *Langmuir*, 31(29):8184–8193, 2015.

[56] John Newman and Karen E Thomas-Alyea. *Electrochemical Systems*. John Wiley & Sons, 2012.

[57] Allen J Bard and Larry R Faulkner. *Electrochemical Methods: Fundamentals and Applications*. John Wiley & Sons, 2001.

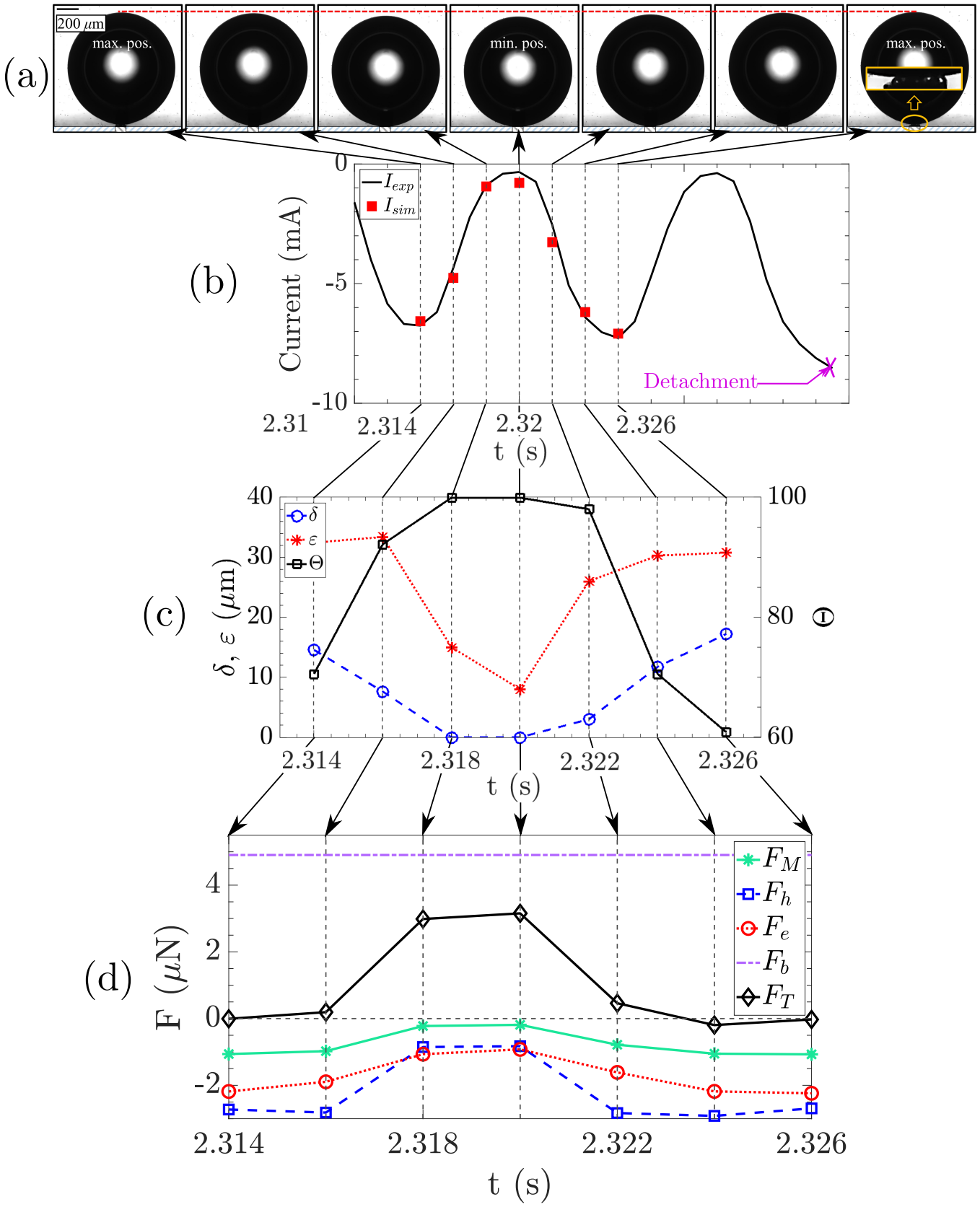

FIG. 9: (a) Consecutive frames from shadowgraphy showing position oscillations of the electrogenerated bubble during one cycle prior to departure, (b) Measured cell current and the simulated cell current at 7 instants of time, (c) Corresponding experimental and simulation parameters, (d) The forces acting on the bubble. For details see text.